Comparisons between molecular dynamics and hydrodynamics treatment of nonstationary thermal processes in a liquid

Hisashi Okumura*
Department of Theoretical Studies, Institute for Molecular Science, Okazaki, Aichi 444-8585, Japan
and Department of Structural Molecular Science, The Graduate University for Advanced Studies, Okazaki, Aichi 444-8585, Japan

David M. Heyes†
Division of Chemistry, School of Biomedical and Molecular Sciences, University of Surrey, Guildford GU2 7XH, United Kingdom
(Received 16 June 2004; published 29 December 2004)

Molecular dynamics (MD) and Navier-Stokes hydrodynamics have been performed to model thermal relaxation processes arising from an initially established nonequilibrium stationary state. A nanoscale two-layer Lennard-Jones (LJ) liquid system was constructed in which the two parts were initially at a different temperature, with a narrow transitional zone between the two layers that was spatially linear in temperature. The highest-temperature layer had widths of five or 20 LJ particle diameters. The hydrodynamics model used parametrized MD-derived transport coefficients and the LJ equation of state as input functions. The temporal and spatial temperature and density profiles produced by the two methods show good agreement, indicating that a hydrodynamics description is reliable even for nonstationary phenomena down to the scale of a few molecular diameters. We found that at certain locations the Navier-Stokes solution predicted that the pressure and temperature profiles relaxed in a damped oscillatory manner, which we could discern despite the fluctuations in the MD data.

DOI: 10.1103/PhysRevE.70.061206 PACS number(s): 66.60.+a, 66.10.Cb, 02.70.Ns, 47.85.Dh

I. INTRODUCTION

In order to study liquid behavior by computer simulation, two methods are frequently used. One method is molecular dynamics (MD) simulation, which applies Newton's equations of motion to an assembly of interacting model molecules. This method is "bottom up," as it uses parameters characteristic of the molecules and the intermolecular forces between them as the starting point. The other method is based on continuum hydrodynamics (HD) equations, such as the Navier-Stokes equation. The transport coefficients of viscosity and heat conductivity, and the equation of state are required to characterize the system in this treatment. In contrast to a MD simulation, the HD approach treats the liquid dynamics from a macroscopic or "top-down" point of view.

An important question is how small does the system have to be before the coarse-grained HD approach breaks down, and MD is required? It is therefore of interest to study whether these two methods provide the same dynamical solution for small systems. There are many studies [1–17] that have compared these two methods for several typical examples of nonequilibrium fluids, such as the Rayleigh-Bénard convection [1–3], the flow pattern behind an obstacle [4,5], and the Poiseuille flow [6–8]. However, most of these studies focused on stationary phenomena. In a stationary system, the time t dependence of any field such as temperature T and mass density ρ in the hydrodynamics is zero (i.e., $\partial T/\partial t=0$, $\partial \rho/\partial t=0$, etc.). There are only a few papers [9–13] that have compared these methods for nonstationary systems. In particular, there is no work in which all five fields of temperature T, mass density ρ, pressure P, potential energy U, and fluid velocity v have been used in the HD calculations, and compared with those produced by a corresponding MD treatment. It is necessary to examine these five fields by both methods in order to make a thorough comparison between the two schemes.

The purpose of this paper is to compare by MD simulation and HD calculation nonequilibrium fluids in stationary and nonstationary cases. In this work we compare all five fields of T, ρ, P, U, and v. As the example of the nonstationary process, we use thermal relaxation from a spatially inhomogeneous system that has high- and low-temperature regions. We have calculated this thermal relaxation process, resolved in space and time, by both MD and HD treatments and for the same initial conditions.

The outline of the present article is as follows. In Sec. II we describe the computational details of the MD simulation and the HD calculation. In Sec. III the results and discussion are presented. Concluding remarks follow in Sec. IV.

II. METHODS

A. Molecular dynamics simulations

We have performed MD simulations using the Lennard-Jones (LJ) 12-6 potential $\phi(r)=4\epsilon\{(\sigma/r)^{12}-(\sigma/r)^6\}$ where ϵ and σ set the energy and length scales of the system, respectively. In the following discussion, the length, the energy, and the mass are scaled in units of the Lennard-Jones diameter σ, the minimum value of the potential ϵ, and the atom mass m. We used an asterisk $(*)$ for reduced quantities such as the reduced length $r^*=r/\sigma$, the reduced temperature T^*

*Electronic address: hokumura@ims.ac.jp
†Electronic address: d.heyes@surrey.ac.uk

$=k_B T/\epsilon$, where k_B is Boltzmann's constant, the reduced pressure $P^*=P\sigma^3/\epsilon$, the reduced mass density $\rho^*=\rho\sigma^3/m$, and the reduced time $t^*=t\sqrt{\epsilon/m\sigma^2}$.

The number of particles N in the cubic unit cell was 100 000, with the usual periodic boundary conditions applied in the x, y, and z directions. The length of the cubic simulation box was $L^*=50$; therefore the volume of the box was $V^*=125\,000$ and the average number density in the whole box was $\rho^*=0.80$. The equations of motion were integrated by the velocity Verlet algorithm, with a time step of $\delta t^*=0.01$. The interaction cutoff radius r_c^* was taken as 4.0, and cutoff corrections were added to the computed pressure and potential energy.

In order to calculate the distribution of the fields such as temperature $T(x,t)$, we resolved the simulation box into 50 segments along the x axis. The fields of temperature T_k, density ρ_k, pressure P_k, potential energy U_k, and fluid velocity v_k along the x direction in the kth slice are determined by

$$T_k=\frac{1}{3k_B N_k}\sum_{i\in k} m(\dot{\mathbf{r}}_i-\dot{\mathbf{r}}_0)^2, \tag{1}$$

$$\rho_k=m\frac{N_k}{V_k}, \tag{2}$$

$$P_k=\frac{1}{3V_k}\sum_{i\in k}\left\{m(\dot{\mathbf{r}}_i-\dot{\mathbf{r}}_0)^2-\frac{1}{2}\sum_{j\neq i} r_{ij}\frac{d\phi(r_{ij})}{dr_{ij}}\right\}, \tag{3}$$

$$U_k=\frac{1}{2N_k}\sum_{i\in k}\sum_{j\neq i}\phi(r_{ij}), \tag{4}$$

$$v_k=\frac{1}{N_k}\sum_{i\in k}\dot{x}_i, \tag{5}$$

where N_k is the number of particles in the kth sliced region, V_k is its volume, $\phi(r_{ij})$ is the interatomic potential for the distance $r_{ij}\equiv|\mathbf{r}_i-\mathbf{r}_j|$ between two particles at $\mathbf{r}_i$ and $\mathbf{r}_j$, and $\dot{\mathbf{r}}_0\equiv(1/N_k)\Sigma_{i\in k}\dot{\mathbf{r}}_i$.

Before realizing the nonstationary thermal process, we had to set up a stationary state containing a high-temperature region and a low-temperature region, with a transitional zone on either side, with T linear in x. The usual periodic boundary conditions were applied in the y and z directions, so the system modeled was a hot-cold layer "sandwich." Velocity rescaling was used to produce the following initial temperature profile:

$$T^*(x^*)=\begin{cases}T_0^*, & 0\le x<x_1^*,\\ (T_1^*-T_0^*)(x^*-x_1^*)/(x_2^*-x_1^*)+T_0^*, & x_1^*\le x<x_2^*,\\ T_1^*, & x_2^*\le x<x_3^*,\\ (T_1^*-T_0^*)(x^*-x_4^*)/(x_3^*-x_4^*)+T_0^*, & x_3^*\le x<x_4^*,\\ T_0^*, & x_4^*\le x\le L^*.\end{cases} \tag{6}$$

In order to investigate the relaxation process in several case studies, we used four sets of values for the parameters (T_0^*, T_1^*, x_1^*, x_2^*, x_3^*, x_4^*, L^*) in Eq. (6), as given in Table I. Systems 1 and 3 have broader high-temperature regions (width of 20) than 2 and 4 (width of 5). Systems 1 and 2 have a bigger difference between high- and low-temperature regions than systems 3 and 4 (ratio of 2.0 and 1.2, respectively). 20 000 MD time steps were performed in systems 1 and 2 ($T_1^*=2.0$) and 10 000 MD time steps in systems 3 and 4 ($T_1^*=1.2$) to establish stationary states. The densities of the layers naturally adjusted to the temperature differences. The time-averaged pressure gradient in the x direction also relaxed to zero in two layers and in the transitional boundary regimes.

TABLE I. Parameters of the temperature control for Eq. (6).

	System 1	System 2	System 3	System 4
T_0^*	1.0	1.0	1.0	1.0
T_1^*	2.0	2.0	1.2	1.2
x_1^*	10.0	17.5	10.0	17.5
x_2^*	15.0	22.5	15.0	22.5
x_3^*	35.0	27.5	35.0	27.5
x_4^*	40.0	32.5	40.0	32.5
L^*	50.0	50.0	50.0	50.0

After achieving the stationary states in these systems, we turned off the temperature control and performed microcanonical MD simulations for 20 000 time steps, i.e., until $t^*=200$, for all parameter sets. We observed the thermal relaxation processes during this phase of the simulation.

B. Hydrodynamics calculations

In order to mimic the MD-generated states by the HD treatment, we solved the following one-dimensional continuum equations:

$$\frac{\partial Q}{\partial t}+\frac{\partial E}{\partial x}+\frac{\partial R}{\partial x}=0. \tag{7}$$

Each term in Eq. (7) is

$$Q=\begin{bmatrix}\rho\\ \rho v\\ e\end{bmatrix},\quad E=\begin{bmatrix}\rho v\\ P+\rho v^2\\ (e+P)v\end{bmatrix},$$

$$R=\begin{bmatrix}0\\ -\left(\frac{4}{3}\eta+\zeta\right)v_x\\ -\left(\frac{4}{3}\eta+\zeta\right)v_x v-\kappa T_x\end{bmatrix}, \tag{8}$$

where $e \equiv \rho[(3/2m)k_B T + (1/m)U + (1/2)v^2]$ is the total energy, η is shear viscosity, ζ is bulk viscosity, κ is thermal conductivity, and the subscripts x of v and T mean the x derivative. The first equation of Eq. (8) introduces the mass conservation. The second equation is the momentum-conservation equation, that is, the Navier-Stokes equation, and the last equation enforces energy conservation.

In order to realize the same initial conditions as in the MD simulation, the side length of the cubic simulation cell was taken as $L^* = 50$, with the usual periodic boundary conditions in all three directions. The space was decomposed into 200 segments along the x axis with an interval of $\Delta x^* = 0.25$ to resolve the HD fields. The temperature distribution was determined as in Eq. (6). The velocity field was $v(x,t) = 0$ because there is no flow in the stationary state of this MD simulation. As a result of the no-flow condition, $v(x,t) = 0$, the pressure should be constant with x (i.e., $\partial P/\partial x = 0$) which is derived from the Navier-Stokes equation (8). The initial values of the fields of T, ρ, P, U, and v were determined to satisfy these conditions. The relationships between T, ρ, P, and U were calculated using Johnson *et al.*'s LJ equation of state [18].

After obtaining the appropriate initial conditions, the time development of the HD fields was computed using the MacCormack algorithm [19]. This algorithm is a predictor-corrector version of the Lax-Wendroff scheme [20,21] with an explicit integrator. It has second-order accuracy in both space and time. It is widely used to solve the Navier-Stokes equation [22–24], which has viscosity and thermal conductivity terms, thus involving simultaneous mass and heat flow.

The state Q^{n+1} at the $(n+1)$th time step is obtained from Q^n at the nth step as follows:

$$Q_l^* = Q_l^n - \frac{\Delta t}{\Delta x}(E_l^n - E_{l-1}^n) - \frac{\Delta t}{\Delta x}(R_{l+1/2}^n - R_{l-1/2}^n), \tag{9}$$

$$Q_l^{n+1} = \frac{1}{2}(Q_l^n + Q_l^*) - \frac{1}{2}\frac{\Delta t}{\Delta x}(E_{l+1}^* - E_l^*) - \frac{1}{2}\frac{\Delta t}{\Delta x}(R_{l+1/2}^n - R_{l-1/2}^n), \tag{10}$$

where the subscript l represents the position of the sliced segments along the x direction. The time step was set to $\Delta t^* = 0.0001$, and these equations were solved for time up to $t^* = 200$ (or 2 000 000 time steps). Note that the HD time step was some 100 times smaller than the MD time step. In order to check the correctness of our HD calculations and investigate the influence of the choices of Δt^* and Δx^*, we also solved the HD equations with different values of $(\Delta t^*, \Delta x^*) = (0.0001, 0.50)$ (0.0002, 0.25), and (0.0002, 0.50). We confirmed that the HD results by these different values of Δt^* and Δx^* are the same as one another. There was no artifact introduced such as artificial oscillations in the fields. This fact shows that our HD calculations by the MacCormack algorithm are reliable.

C. Calculations of the transport coefficients

The transport coefficients of η, ζ, and κ are necessary for the HD calculations [25–35]. These transport coefficients were determined by the appropriate Green-Kubo formula [25–27]. For the shear viscosity we have,

$$\eta = \frac{V}{k_B T}\int_0^\infty dt \langle P_{\alpha\beta}(t) P_{\alpha\beta}(0)\rangle, \tag{11}$$

where

$$P_{xy} = \frac{1}{V}\sum_i \left\{ m\dot{x}_i\dot{y}_i - \frac{1}{2}\sum_{j\neq i}\frac{x_{ij}y_{ij}}{r_{ij}}\frac{d\phi(r_{ij})}{dr_{ij}} \right\}. \tag{12}$$

For the bulk viscosity,

$$\zeta = \frac{V}{k_B T}\int_0^\infty dt \langle \delta P(t)\delta P(0)\rangle, \tag{13}$$

where

$$\delta P = \frac{1}{3V}\sum_i \left\{ m\dot{r}_i^2 - \frac{1}{2}\sum_{j\neq i} r_{ij}\frac{d\phi(r_{ij})}{dr_{ij}} \right\} - \langle P\rangle. \tag{14}$$

For the longitudinal viscosity,

$$\frac{4}{3}\eta + \zeta = \frac{V}{k_B T}\int_0^\infty dt \langle \delta P_{\alpha\alpha}(t)\delta P_{\alpha\alpha}(0)\rangle, \tag{15}$$

where

$$\delta P_{xx} = \frac{1}{V}\sum_i \left\{ m\dot{x}_i^2 - \frac{1}{2}\sum_{j\neq i}\frac{x_{ij}^2}{r_{ij}}\frac{d\phi(r_{ij})}{dr_{ij}} \right\} - \langle P_{xx}\rangle. \tag{16}$$

For thermal conductivity,

$$\kappa = \frac{V}{k_B T^2}\int_0^\infty dt \langle J_\alpha(t) J_\alpha(0)\rangle, \tag{17}$$

where

$$J_x = \frac{1}{2V}\sum_i \left[\dot{x}_i \left\{ m\dot{r}_i^2 + \sum_{j\neq i}\phi(r_{ij}) \right\} - \sum_{j\neq i}\dot{\mathbf{r}}_i \cdot \mathbf{r}_{ij}\frac{x_{ij}}{r_{ij}}\frac{d\phi(r_{ij})}{dr_{ij}} \right]. \tag{18}$$

Here for two molecules i and j, $x_{ij} \equiv |x_i - x_j|$, where x_i is the x component of the coordinate $\mathbf{r}_i$, and $\langle\cdots\rangle$ means a microcanonical ensemble average.

The autocorrelation functions were calculated from microcanonical MD simulations carried out at several temperatures between $T^* = 1.0$ and 2.0 and densities between $\rho^* = 0.60$ and 0.90. The cutoff radius r_c^* was 4.0 and a cutoff correction was included in the pressure tensor. The number of particles N was 1000. The equations of motion were integrated by the velocity Verlet algorithm for 2 000 000 MD

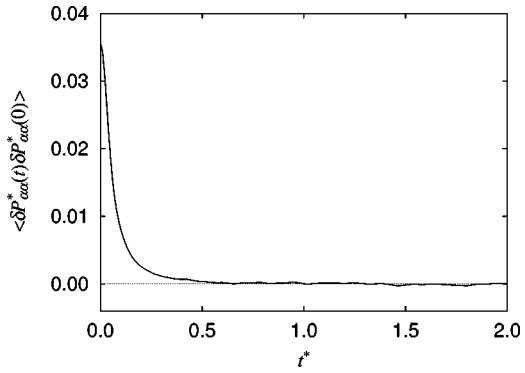

FIG. 1. Autocorrelation function $\langle \delta P^*_{\alpha\alpha}(t)\delta P^*_{\alpha\alpha}(0)\rangle$ at $\rho^*=0.80$ and $T^*=1.0$.

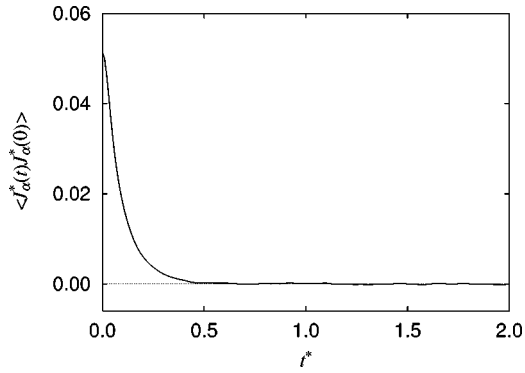

FIG. 2. Autocorrelation function $\langle J^*_\alpha(t)J^*_\alpha(0)\rangle$ at $\rho^*=0.80$ and $T^*=1.0$.

steps. The time step Δt^* was reduced with increasing density, between $\Delta t^*=0.005$ and 0.010. The 2 000 000 step-simulation results were divided into segments of 200 MD steps. We calculated the autocorrelation functions in each segment and took the averages from all such segments and directions, $\alpha=x, y, z$. The autocorrelation functions were integrated numerically to obtain the transport coefficients. For the purpose of estimating the error bars for the transport coefficients, we carried out the above procedure starting from five different initial conditions. That is, we performed the MD simulations for 10 000 000 steps in total at each density and temperature. The error bars were determined as the standard deviation from these five different initial conditions.

An example of the autocorrelation function $\langle \delta P^*_{\alpha\alpha}(t)\delta P^*_{\alpha\alpha}(0)\rangle$ is shown in Fig. 1 and $\langle J^*_\alpha(t)J^*_\alpha(0)\rangle$ in Fig. 2 for the state point $\rho^*=0.80$ and $T^*=1.0$. These autocorrelation functions are statistically zero at $t^*=1.0$, which is necessary for the transport coefficients to be correctly determined.

The values of the transport coefficients are given in Table II. The longitudinal viscosity is calculated in two ways. One method is a determination from Eqs. (11) and (13) and the other one is from Eq. (15). Table II shows the longitudinal-viscosity values from the two methods, which agree well within their error bars at every density and temperature (a useful self-consistency check). In the HD calculations, we used the values determined from Eq. (15) with a linear interpolation for intermediate ρ^* and T^* values. The error bars in the transport coefficients are less than 5%. In order to check the effect of the transport-coefficient error, we also per-

TABLE II. Transport coefficients of Lennard-Jones 12-6 potential. Longitudinal viscosity $4\eta^*/3+\zeta^*$ obtained (a) from Eqs. (11) and (13) and (b) from Eq. (15). The numbers in parentheses are the estimated uncertainties.

				$4\eta^*/3+\zeta^*$		
ρ^*	T^*	η^*	ζ^*	(a)	(b)	κ^*
0.60	1.5	0.81(4)	0.72(6)	1.80(7)	1.80(6)	3.51(5)
0.60	2.0	0.863(9)	0.533(29)	1.68(4)	1.71(7)	3.80(13)
0.65	1.5	1.03(5)	0.65(5)	2.02(6)	1.98(10)	4.17(16)
0.65	2.0	1.030(29)	0.55(6)	1.92(9)	1.91(6)	4.39(12)
0.70	1.0	1.20(6)	1.01(4)	2.61(9)	2.68(12)	4.50(18)
0.70	1.5	1.21(8)	0.76(4)	2.37(12)	2.29(6)	4.95(15)
0.70	2.0	1.235(23)	0.62(5)	2.27(6)	2.30(9)	5.30(16)
0.75	1.0	1.52(6)	0.92(11)	2.95(11)	3.01(18)	5.32(26)
0.75	1.5	1.52(11)	0.77(8)	2.79(8)	2.81(3)	5.92(11)
0.75	2.0	1.51(4)	0.65(8)	2.66(13)	2.70(13)	6.14(17)
0.80	1.0	2.05(8)	0.81(5)	3.55(8)	3.57(11)	6.3(3)
0.80	1.5	1.97(7)	0.75(7)	3.39(16)	3.30(12)	6.94(27)
0.80	2.0	1.862(27)	0.65(7)	3.13(7)	3.18(9)	7.11(24)
0.85	1.0	2.76(13)	0.873(25)	4.55(16)	4.64(19)	7.9(3)
0.85	1.5	2.54(5)	0.691(25)	4.07(4)	4.06(7)	8.07(16)
0.90	1.0	4.0(3)	0.94(9)	6.3(4)	6.33(13)	8.76(21)
0.90	1.5	3.25(10)	0.79(7)	5.12(17)	5.11(11)	9.40(25)

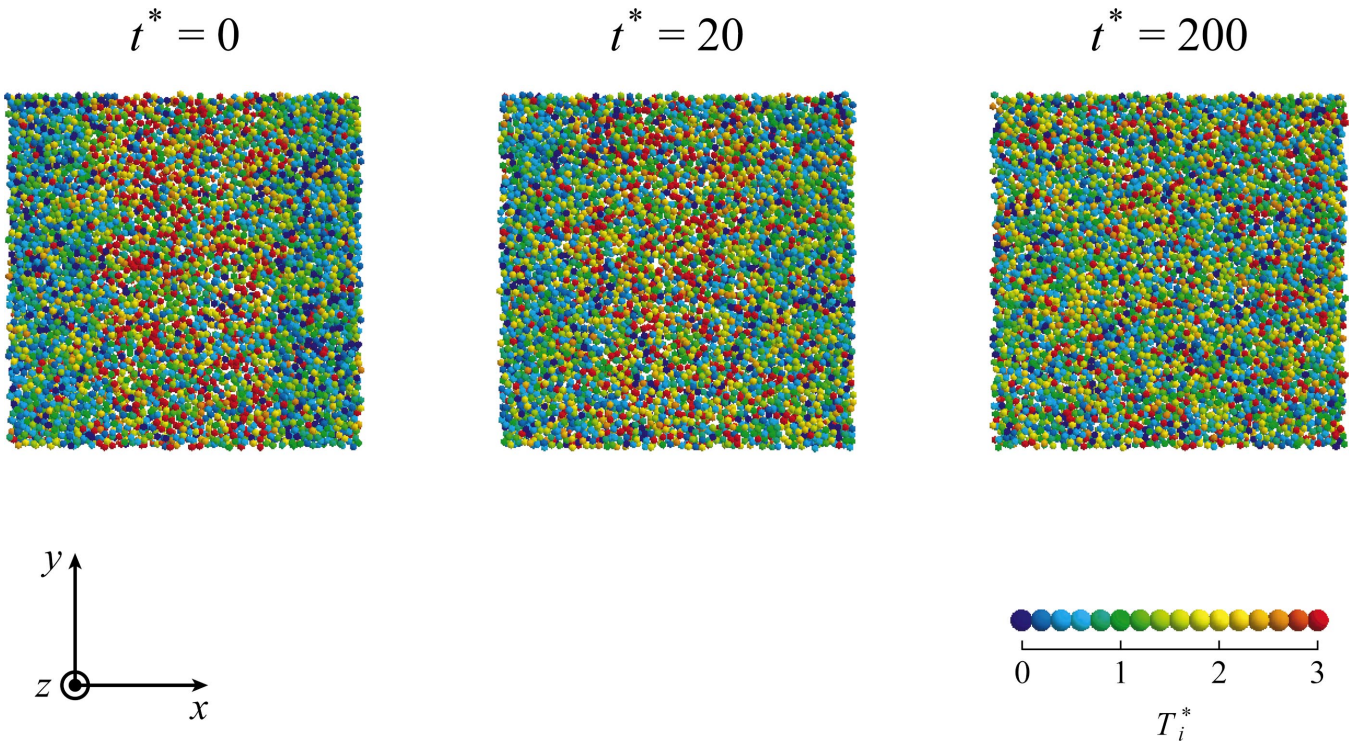

FIG. 3. (Color) Snapshots of atoms during the thermal relaxation process in the MD system 1. Each atom color depends on its temperature.

formed the HD calculation with transport coefficients differing by 5%.

III. RESULTS AND DISCUSSION

In order to gain some insights into the nature of the thermal relaxation on the molecular scale, the data from the MD system 1 are shown in Fig. 3. This figure gives snapshots showing only the atoms that fall within an xy layer that is 6% of the box side length thick in the z direction. The color coding indicates the kinetic energy or "temperature" $T_i \equiv m\dot{r}_i^2/3k_B$ of each atom i. At the stationary state $t^*=0.0$, many of the atoms in the high-temperature region near the center are in the red–yellow color range. Many of the atoms in the low-temperature region near the boundary of $x^*=0$ and $x^*=L^*$ are in the blue–green color range. Because the pressure at the stationary state is, within statistics, constant across the box in the x direction, i.e., $\partial P/\partial x=0$, the density is low in the high-temperature region and high in the low-temperature region. This can be seen in Fig. 3 for the system at $t^*=0$. The high-temperature region of the cell is relatively sparsely populated compared with the cold regions. During the nonstationary phase of the simulation, the distributions of T and ρ can be seen to be relaxing toward a spatially uniform value as shown in the snapshots at $t^*=20$. Finally, after a simulation time of $t^*=200$, the system has essentially finished relaxing to a uniform distribution of particles throughout the cell.

Figures 4–7 show the distributions of the five fields of T^*, ρ^*, P^*, U^*, and v^* in the systems 1–4, respectively. Each system has the temperature distribution given in Eq. (6) at $t^*=0$. The highest temperature in Figs. 4 and 5 is $T_1^*=2.0$, while that in Figs. 6 and 7 is $T_1^*=1.2$. The width of the highest-temperature layer in Figs. 4 and 6 is 20, and that in Figs. 5 and 7 is 5. These figures show that the density in the high-temperature region is lower than in the low-temperature region. The potential energy in the high-temperature region is higher than that in the low-temperature region. The density and potential energy are functions of temperature and pressure. As the system is stationary, the pressure is constant across the system, and therefore the density and potential energy are solely dependent on the local temperature. The average velocity at each point is also zero at $t^*=0$. It can be seen that the stationary results by MD and HD calculations agree very well. Note that there are statistical fluctuations in the MD data, which are absent in the HD method. All fields determined by the MD simulations have fluctuations because they are calculated from a finite number of atoms and finite number of realizations of the relaxation event.

After removing the velocity scaling, relaxation toward a new steady state can be observed. The distribution of T^*, ρ^*, and U^* becomes progressively flatter as time passes. The profiles of P^* and v^* reflect the predominant flows during relaxation. All distributions are flat on completion of the simulation. We can conclude therefore that the MD and HD calculations represent well the state of the system at all stages of the relaxation process.

We also checked the effect of small changes in the values of the transport coefficients on the relaxation profiles produced by the HD method, using values at the extremes of the uncertainty bars. We found that the changes in the HD prop-

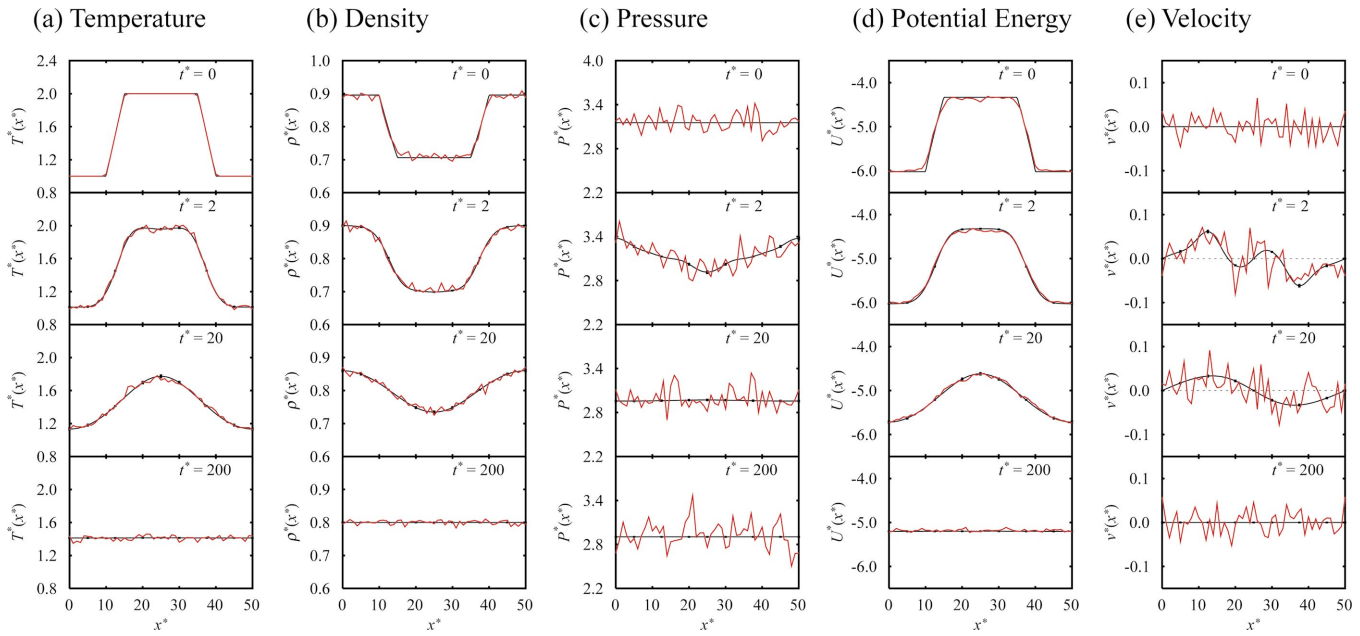

FIG. 4. (Color) Distributions of T^*, ρ^*, P^*, U^*, and v^* for system 1 at $t^* = 0$, 2, 20, and 200. Red and (smoother) black lines are obtained by the MD simulation and the HD calculations, respectively.

erty profiles were much less than the fluctuations of the MD simulations. We also carried out HD calculations of the relaxation using constant values for the transport coefficients. In this case, the agreement was not so good, which can be appreciated by the relatively large variation of the transport coefficient values (typically by factors of 2 or 3) in the relevant density and temperature range, as shown in Table II.

Figures 8–11 show the time development of each field at certain values of x. They are at the center of the low-temperature region $x^* = 0$, the center of the high-temperature region $x^* = 25$, and the middle of the transitional temperature regions, taken as $x^* = 12.5$ for the systems 1 (Fig. 8) and 3 (Fig. 10) and at $x^* = 20$ for the systems 2 (Fig. 9) and 4 (Fig. 11). The relaxation in the high-temperature region starts from $T^* = 2.0$ in Fig. 8 and Fig. 9 and from $T^* = 1.2$ in Fig. 10 and Fig. 11. A microscopic system always has fluctuations on a shorter time scale than that characteristic of the macroscopic HD relaxation. In Figs. 8–11 the red lines of the MD simulations in all fields show these microscopic fluctuations. They fluctuate around the black lines of the HD calculations. In order to compare the MD and HD profiles on the basis of more comparable fluctuations, we also took local time aver-

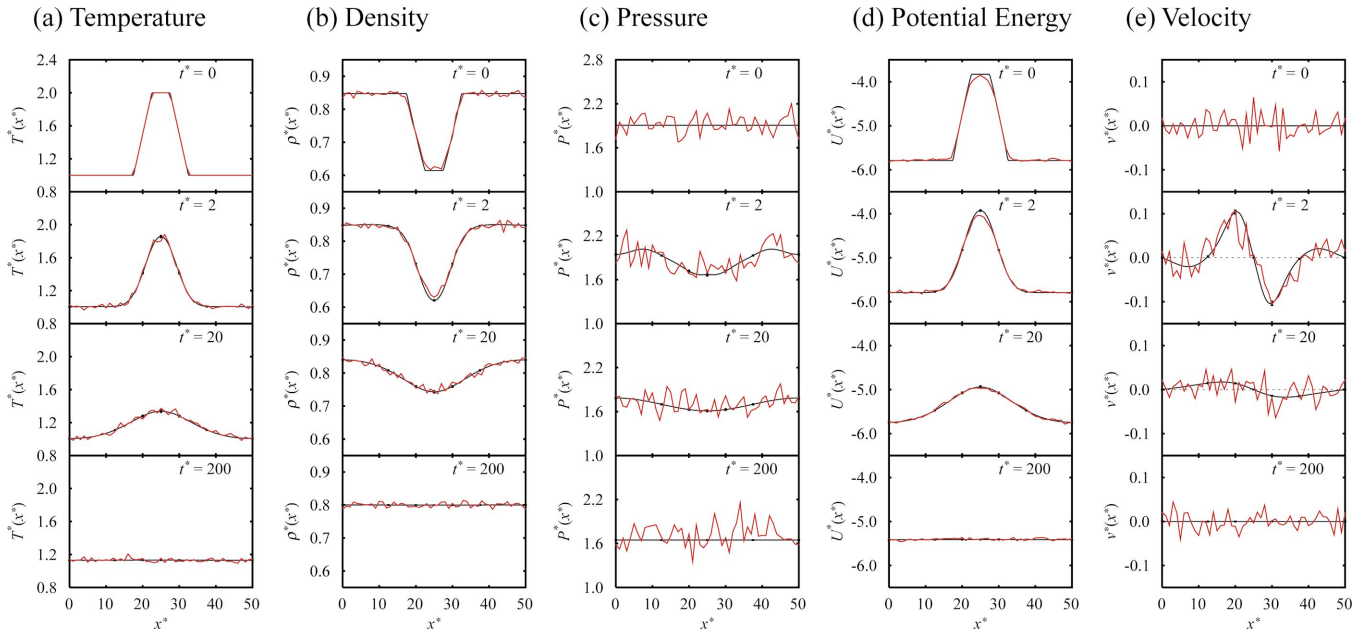

FIG. 5. (Color) Distributions of T^*, ρ^*, P^*, U^*, and v^* for system 2. See the caption of Fig. 4 for further details.

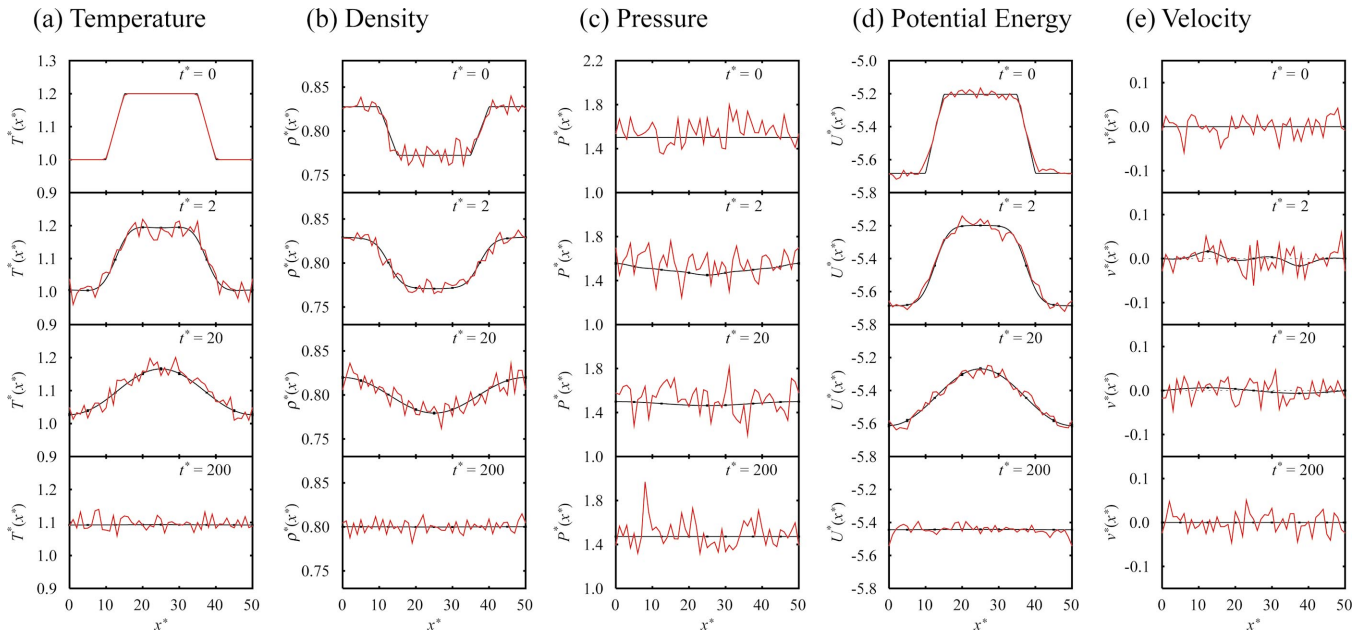

FIG. 6. (Color) Distributions of T^*, ρ^*, P^*, U^*, and v^* for system 3. See the caption of Fig. 4 for further details.

ages of all the MD fields in blocks of $100\delta t^* = 1.0$. This alleviated the fluctuations in the MD data. This time resolution is now longer than the time scale of these microscopic fluctuations but shorter than that of macroscopic HD behavior. These time averages are shown as blue lines in Figs. 8–11. As the fluctuations of the time-average fields are now much smaller than those of instantaneous values, it can be seen that the relaxation processes of all fields produced by the MD and HD methods agree well at every position. In particular, the HD fields agree with the time-average MD fields much better than with the instantaneous MD fields. Our results indicate that the HD calculation based on the Navier-Stokes continuum equations is essentially satisfied even for such small and nonstationary systems. Our system size of $L^* = 50$ corresponds to $L = 17$ nm in the case of argon.

As we discussed above, the agreement of the MD and HD treatments is very good. There are slight differences, however. The potential energy in the system 2 at $t^* = 0-2$ and in the region of $x^* = 22-28$ obtained by the MD simulation is less than that of the HD calculation as shown in Fig. 5(d). This difference can be understood as follows. The curvature of the temperature and density profiles in system 2 in these regions is the largest of the four systems as shown in Fig. 5(a) and in Fig. 5(b), respectively. The MD potential energy

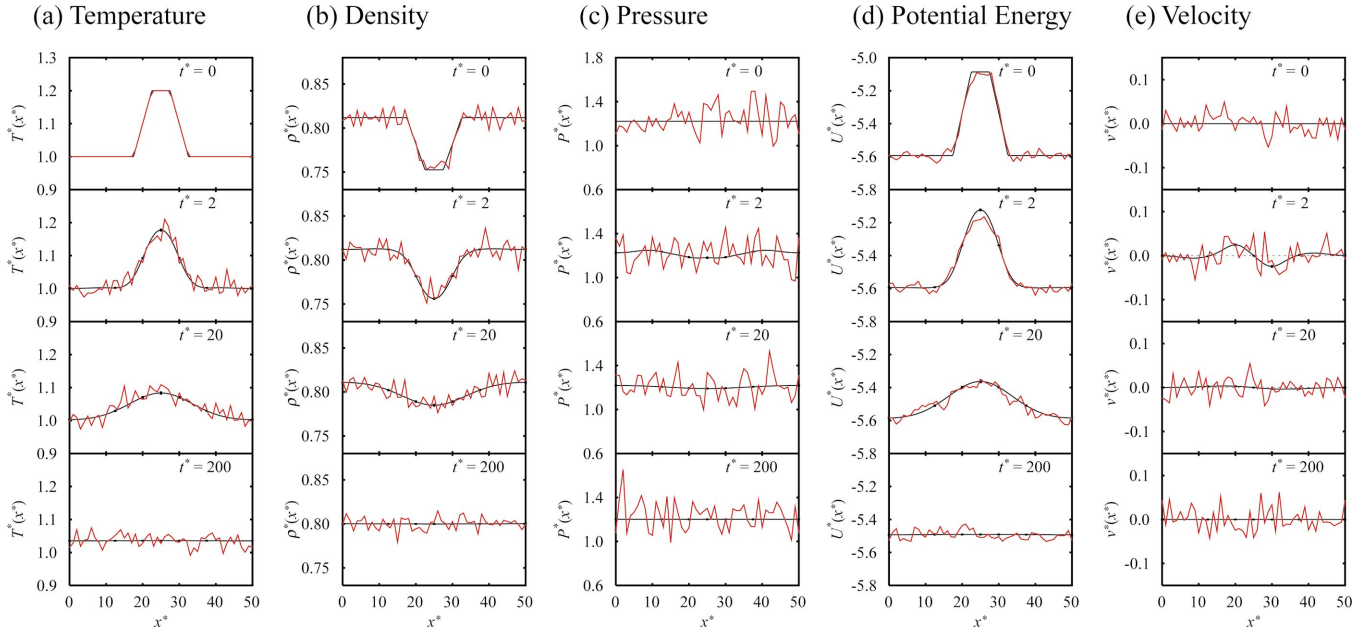

FIG. 7. (Color) Distributions of T^*, ρ^*, P^*, U^*, and v^* for system 4. See the caption of Fig. 4 for further details.

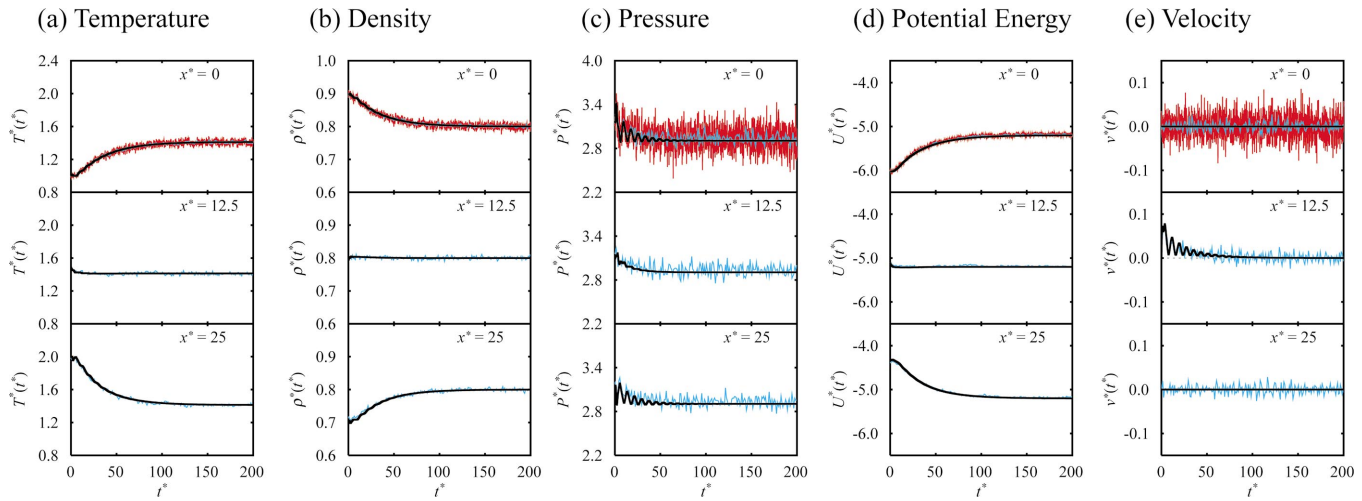

FIG. 8. (Color) Time development of T^*, ρ^*, P^*, U^*, and v^* for system 1 at $x^*=0$, 12.5, and 25. Red lines are the instantaneous MD data, blue lines are the time average of MD data taken in each interval of $100\delta t^*=1.0$, and (smoother) black lines are obtained by the HD calculation. In the cases of $x^*=12.5$ and 25, the instantaneous MD data are not illustrated to show the time-average MD results clearly.

value clearly depends on the surrounding temperature and density distributions. On the other hand, the HD potential energy value is estimated from the equation of state using the temperature and density value at a given location. In regions where the local density is decreasing rapidly from a plateau value, the HD approach will overestimate the average local particle density and hence the potential energy and pressure. This problem could be alleviated by using an average local density in the HD treatment, as is done in, for example, the density functional approach, e.g., [36].

The velocities v^* at $x^*=0$ and 25 are zero at all times in the MD and HD calculations as shown in Figs. 4(e)–11(e). The net fluid flow is in the opposite direction on either side of the centerline. The differences between the field values of T^*, ρ^*, and U^* at the beginning and end of the relaxation at the middle of the transitional temperature region ($x^*=12.5$) in Fig. 8 (system 1) are smaller than those at this middle point ($x^*=20$) in Fig. 9 (system 2). The situation is much the same on comparing Fig. 10 (system 3) and Fig. 11 (system 4). This feature is clearly caused by the difference in the widths of the low- and high-temperature plateau between systems 1 and 2, and 3 and 4. (The width of the transitional temperature zone is the same in each case.) The width of the high-temperature region is the same as that of the low-temperature region in the systems 1 and 3. (Both layers have a width of 20.) Therefore, the temperature changes very little in the middle of the transitional temperature region. On the other hand, in the systems 2 and 4, the width of the high-temperature region is 5 and smaller than that of the low-temperature region which is 35. These values consequently change more in the systems 2 and 4, even at the middle of the transitional temperature region.

In Figs. 8–11, a damped oscillatory decay can be seen for some of the data generated by the HD method. In particular,

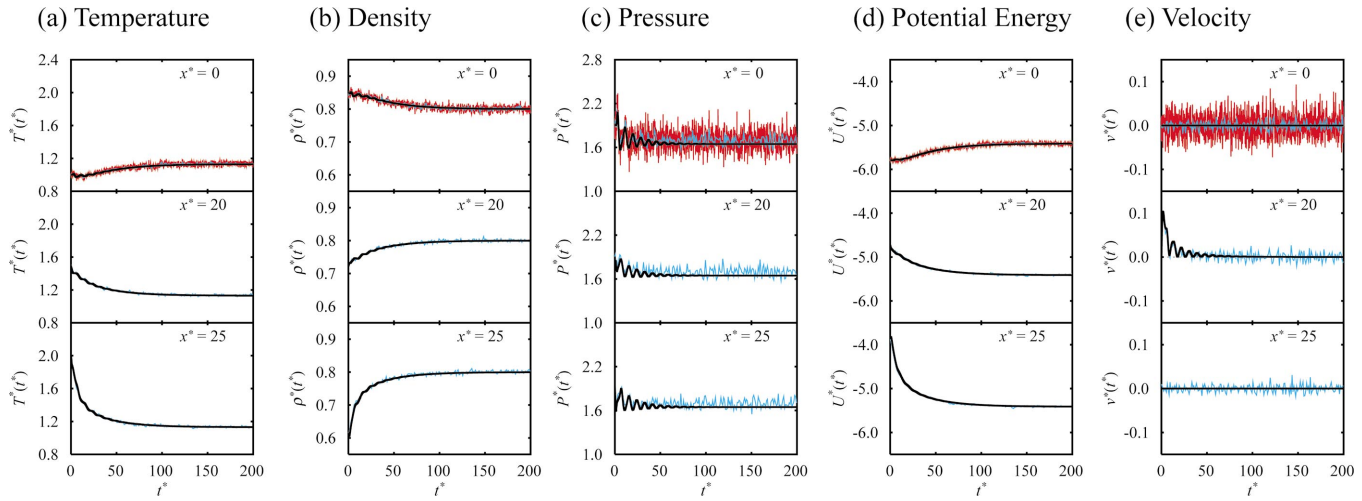

FIG. 9. (Color) Time development of T^*, ρ^*, P^*, U^*, and v^* for system 2 at $x^*=0$ 20, and 25. See the caption of Fig. 8 for further details.

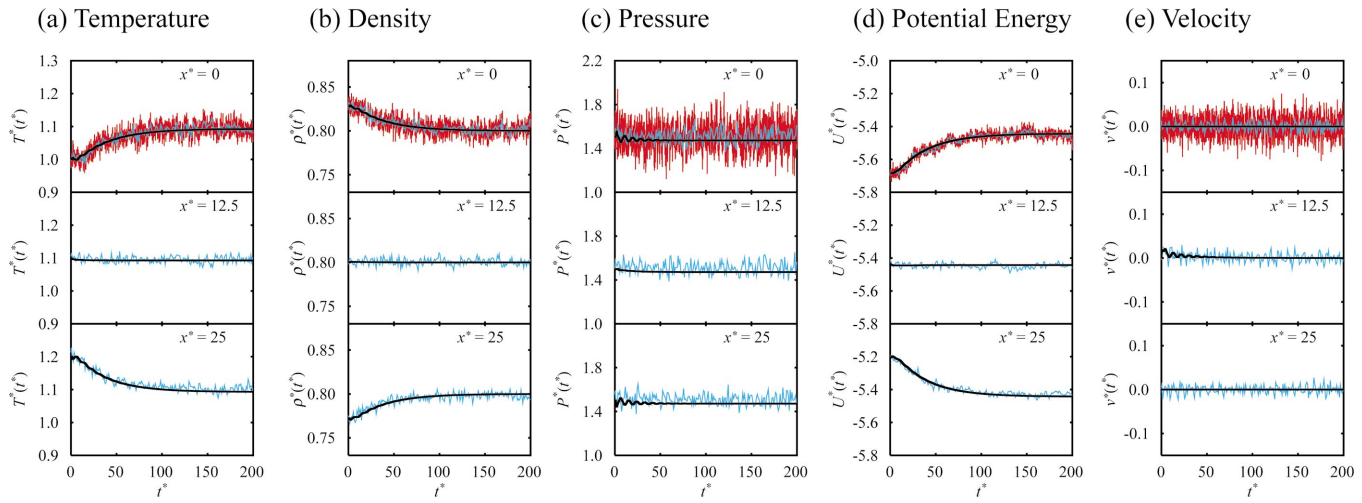

FIG. 10. (Color) Time development of T^*, ρ^*, P^*, U^*, and v^* for system 3 at $x^*=0$, 12.5, and 25. See the caption of Fig. 8 for further details.

notice the oscillations of v^* at $x^*=12.5$ in the system 1 and 3 and at $x^*=20$ in the system 2 and 4 and those of P^* at these and other locations. In order to characterize these oscillations in more detail, we show all fields at $x^*=20$ of the system 2 obtained by the HD calculations (black lines) for the initial part of the decay in Fig. 12. The temperature T^* and density ρ^* also have oscillations, in phase with P^*, while U^* does not have such a clear oscillation behavior. The velocity is substantially out of phase with the P^* data. All fields of instantaneous MD data (red lines) and those of the time-average MD data (blue lines) in the time interval of $100\delta t^*$ are also shown in Fig. 12. Fluctuations are inherent features of the MD method, and these oscillations are relatively difficult to discern within the noise in the instantaneous MD data. However, taking a time average of the MD data makes it easier to detect these HD oscillations in the MD results as well. The time averages of P^* and v^* in the MD data show clearly very similar oscillations to those of HD calculations. The time averages of T^* and ρ^* also indicate the oscillations as the HD results, although they are not as clear as P^* and v^*. The time average of U^* does not have such an oscillation. This is also consistent with the HD treatment. A possible reason for these oscillations is as follows. The heat flows outward from the centerline, because the temperature in the center region is higher than the surroundings. At the same time, there is a fluid flow toward the center because the density in the center region is lower than the surroundings. An initial outward heat flow causes T^* and P^* in the center region to decrease initially. Then there is a net inward flow from the colder regions, reflected in the v^* data, which causes the P^* in the center region to increase again and also makes ρ^* in the center region increase somewhat. This increase of ρ^* acts to reduce the rate of the temperature reduction, in fact the temperature is almost constant for a while. The inward fluid-flow velocity v^* progressively decreases and there is an inversion of P^* and v^*; P^* and T^* in the center region decrease again because the outward heat flow starts to dominate over the inward fluid flow. This process is repeated so that P^* and v^* relax in a damped oscillatory manner out of phase with each other. The pressure and

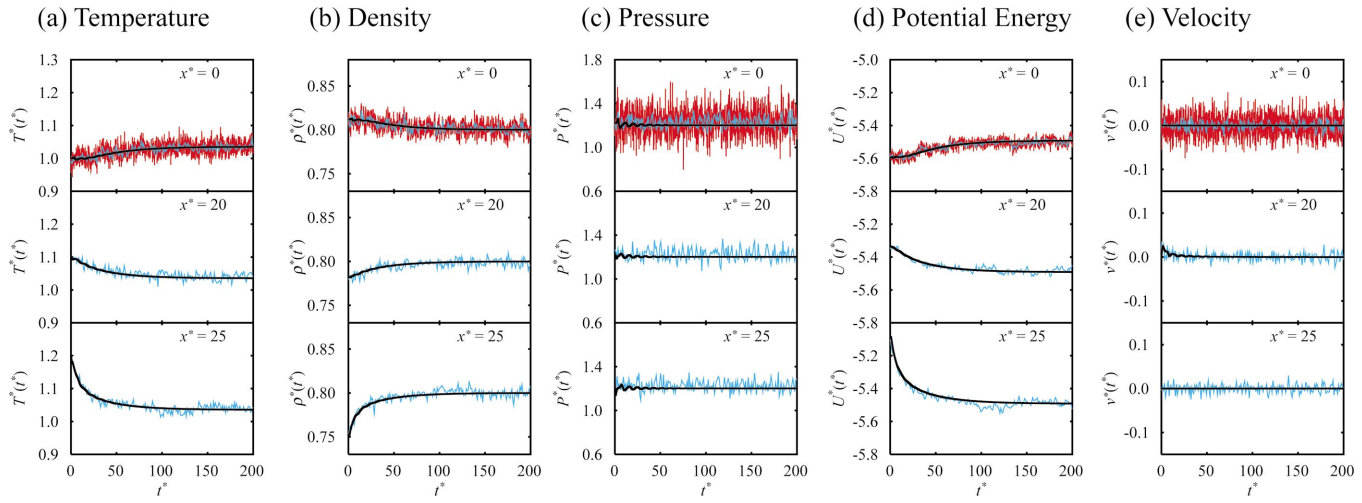

FIG. 11. (Color) Time development of T^*, ρ^*, P^*, U^*, and v^* for system 4 at $x^*=0$, 20, and 25. See the caption of Fig. 8 for further details.

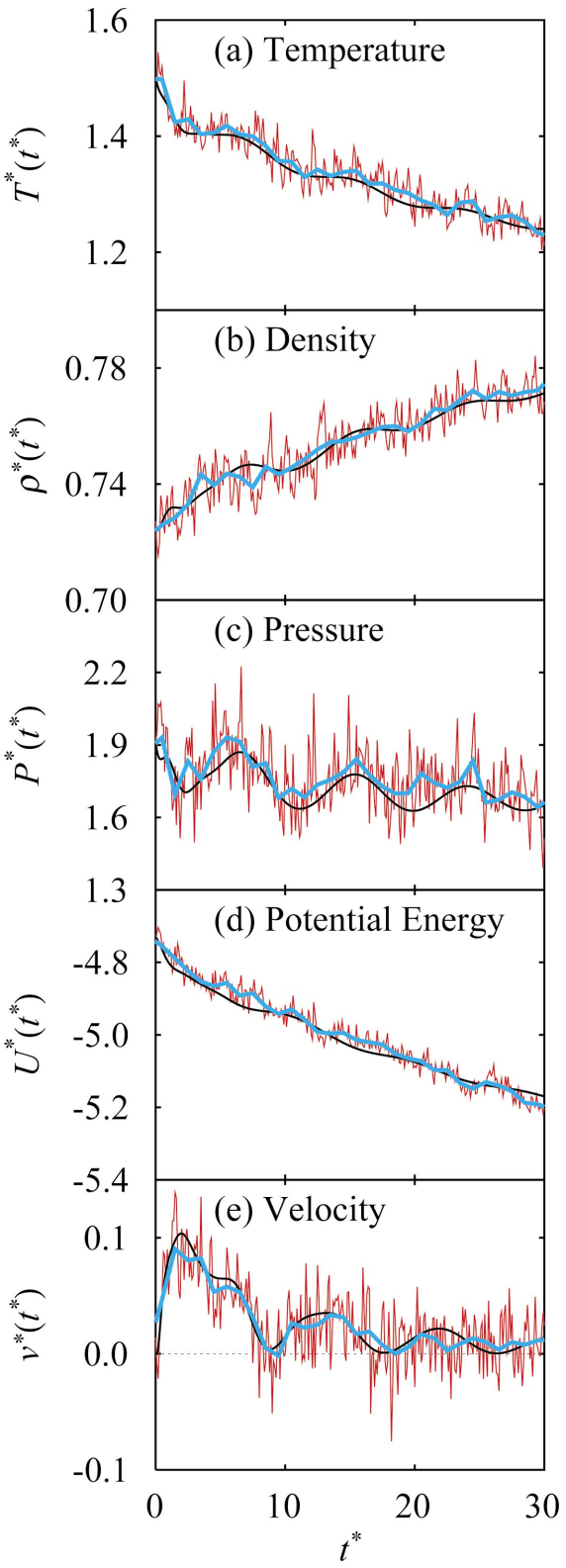

FIG. 12. (Color) The fields T^*, ρ^*, P^*, U^*, and v^* for system 2 at $x^*=20$ during $t^*=0-30$ reduced time units. Red lines are the instantaneous MD data, blue lines are the time average of MD data taken in each interval of $100\delta t^*=1.0$, and (smoother) black lines are obtained by the HD calculation.

velocity oscillations we think are therefore the result of a balance between the inward flow of fluid caused by the density relaxation and the outward heat flow caused by the temperature relaxation. In this process, T^* and ρ^* oscillate in phase with P^*. Because U^* is an increasing function of T^*, and a decreasing function of ρ^*, the contributions of the T^* and ρ^* oscillations to U^* tend to cancel out. As a result, U^* is a relatively smooth monotonically decaying function.

IV. CONCLUSIONS

We have investigated hydrodynamic effects on the nanoscale using molecular and coarse-grained continuum level descriptions of a Lennard-Jones potential fluid. The particular transient effect we considered was thermal relaxation from an initial inhomogeneous temperature distribution. We performed molecular dynamics simulations and solved the Navier-Stokes equation for systems of various initial temperature profiles. We made a systematic comparison between the spatial and temporal variations in T, ρ, P, U, and v for the MD and HD methods. The fields from the two techniques agreed well with each other provided that the equation of state and transport coefficients (shear and bulk viscosity and thermal conductivity obtained from separate simulations) are made functions of density and temperature.

These results strongly suggest that the Navier-Stokes description is reliable down to the nanometer scale not only for stationary case, but also for nonstationary phenomena. Of course we have only considered thermal relaxation, and one would need to consider other processes, such as shear flow, to further validate this conclusion in all its generality. One could argue, based on this result, that for certain systems, MD could be replaced by the continuum approach to study nonstationary liquid behavior, considerably reducing the computational cost. The continuum method is also effective at highlighting quite subtle transients in the temporal behavior of the fields (such as damped oscillations manifest in the pressure and velocity at certain locations in the system) that are obscured by the MD noise. Although the MD simulations produce local fields fluctuations that are inherent to what is a truly microscopic system, by taking a local or "block" time average, we were able to detect the subtle transients observed in the hydrodynamic results. The Navier-Stokes solver can be used on length scales up from the nanoscale, and can be "tuned" to suit the length or time scale of interest. One could see this approach being useful in the area of microfluidics device design, for instance.

ACKNOWLEDGMENTS

H.O. would like to thank Professor N. Ito for useful discussions at the early stage of the present work. This work was supported in part by Grants-in-Aid from the Japan Society for the Promotion of Science and the Royal Society (London) under their visitor exchange scheme. Funding for the NAREGI Nanoscience Project and for Scientific Research in Priority Areas, "Water and Biomolecules," from the Ministry of Education, Culture, Sports, Science and Technology, Japan is gratefully acknowledged.

[1] D. C. Rapaport, Phys. Rev. Lett. **60**, 2480 (1988).
[2] M. Mareschal, M. Malek Mansour, A. Puhl, and E. Kestemont, Phys. Rev. Lett. **61**, 2550 (1988).
[3] A. Puhl, M. M. Mansour, and M. Mareschal, Phys. Rev. A **40**, 1999 (1989).
[4] D. C. Rapaport, Phys. Rev. A **36**, 3288 (1987).
[5] S. T. Cui and D. J. Evans, Mol. Simul. **9**, 179 (1992).
[6] K. P. Travis, B. D. Todd, and D. J. Evans, Phys. Rev. E **55**, 4288 (1997).
[7] D. Risso and P. Cordero, Phys. Rev. E **58**, 546 (1998).
[8] K. P. Travis and K. E. Gubbins, J. Chem. Phys. **112**, 1984 (2000).
[9] D. C. Rapaport, Phys. Rev. A **43**, 7046 (1991).
[10] J. Bougie, S. J. Moon, J. B. Swift, and H. L. Swinney, Phys. Rev. E **66**, 051301 (2002).
[11] H. Okumura and N. Ito, Phys. Rev. E **67**, 045301 (2003).
[12] D. Hirshfeld and D. C. Rapaport, Phys. Rev. Lett. **80**, 5337 (1998).
[13] D. Hirshfeld and D. C. Rapaport, Phys. Rev. E **61**, R21 (2000).
[14] B. L. Holian, W. G. Hoover, B. Moran, and G. K. Straub, Phys. Rev. A **22**, 2798 (1980).
[15] D. R. J. Monaghan and G. P. Morriss, Phys. Rev. E **56**, 476 (1997).
[16] J. Delhommelle, J. Petravic, and D. J. Evans, J. Chem. Phys. **119**, 11005 (2003).
[17] K. Kadau, T. C. Germann, N. G. Hadjiconstantinou, P. S. Lomdahl, G. Dimonte, B. L. Holian, and B. J. Alder, Proc. Natl. Acad. Sci. U.S.A. **101**, 5851 (2004).
[18] J. K. Johnson, J. A. Zollweg, and K. E. Gubbins, Mol. Phys. **78**, 591 (1993).
[19] R. W. MacCormack, AIAA Pap. **69**, 354 (1969).
[20] P. Lax, Commun. Pure Appl. Math. **7**, 159 (1954).
[21] P. Lax and B. Wendroff, Commun. Pure Appl. Math. **13**, 217 (1960).
[22] T. M. Liou, S. H. Chen, and P. W. Hwang, J. Fluids Eng. **124**, 81 (2002).
[23] B. Li, J. Waterw., Port, Coastal, Ocean Eng. **127**, 16 (2001).
[24] S. S. Gokhale and R. Suresh, Int. J. Numer. Methods Fluids **25**, 599 (1997).
[25] J.-H. Hansen and I. R. McDonald, *Theory of Simple Liquids* (Academic, London, 1986), Chap. 8, p. 253.
[26] C. Hoheisel, J. Chem. Phys. **86**, 2328 (1987).
[27] C. Hoheisel, R. Vogelsang, and M. Schoen, J. Chem. Phys. **87**, 7195 (1987).
[28] K. Tankeshwar, K. N. Pathak, and S. Ranganathan, J. Phys.: Condens. Matter **8**, 10 847 (1996).
[29] D. M. Heyes, Can. J. Phys. **64**, 774 (1986).
[30] D. M. Heyes, J. Chem. Soc., Faraday Trans. 2 **80**, 1363 (1984).
[31] W. G. Hoover, D. J. Evans, R. B. Hickman, A. J. C. Ladd, W. T. Ashurst, and B. Moran, Phys. Rev. A **22**, 1690 (1980).
[32] W. G. Hoover, A. J. C. Ladd, R. B. Hickman, and B. L. Holian, Phys. Rev. A **21**, 1756 (1980).
[33] H. Okumura and F. Yonezawa, J. Phys. Soc. Jpn. **71**, 685 (2002).
[34] H. Okumura and F. Yonezawa, J. Chem. Phys. **116**, 7400 (2002).
[35] H. Okumura and F. Yonezawa, Phys. Rev. E **67**, 021205 (2003).
[36] S. Punnathanam and D. S. Corti, J. Chem. Phys. **119**, 10 224 (2003).